

Research article

Dmitry Yu. Fedyanin*, Alexey V. Krasavin, Aleksey V. Arsenin and Anatoly V. Zayats

Lasing at the nanoscale: coherent emission of surface plasmons by an electrically driven nanolaser

<https://doi.org/10.1515/nanoph-2020-0157>

Received February 28, 2020; accepted June 26, 2020;

published online July 20, 2020

Abstract: Plasmonics offers a unique opportunity to break the diffraction limit of light and bring photonic devices to the nanoscale. As the most prominent example, an integrated nanolaser is a key to truly nanoscale photonic circuits required for optical communication, sensing applications and high-density data storage. Here, we develop a concept of an electrically driven subwavelength surface-plasmon-polariton nanolaser, which is based on a novel amplification scheme, with all linear dimensions smaller than the operational free-space wavelength λ and a mode volume of under $\lambda^3/30$. The proposed pumping approach is based on a double-heterostructure tunneling Schottky barrier diode and gives the possibility to reduce the physical size of the device and ensure in-plane emission so that the nanolaser output can be naturally coupled to a plasmonic or nanophotonic waveguide circuitry. With the high energy efficiency (8% at 300 K and 37% at 150 K), the output power of up to 100 μ W and the ability to operate at room temperature, the proposed surface plasmon polariton nanolaser opens up new avenues in diverse application areas, ranging from ultrawideband optical communication on a chip to low-power nonlinear

photronics, coherent nanospectroscopy, and single-molecule biosensing.

Keywords: integrated nanolaser; plasmonics; surface plasmon polariton amplification.

1 Introduction

Nanophotonics is ubiquitous in many applications ranging from optical interconnects and sensing to high-density data storage and information processing [1–6]. Particularly, the plasmonic approach offers an opportunity to deal with photonic signals at the nanoscale via coupling to the free-electron oscillations in a metal. It can provide ultracompact components for optical interconnects such as modulators, photodetectors, waveguides and incoherent and coherent nanoscale optical sources [7–13]. The implementation of the latter is a great challenge since a significant amount of the surface plasmon field is concentrated in the metal that results in high Joule losses. Nevertheless, the idea of SPASER (from surface plasmon amplification by stimulated emission radiation) [14, 15] was proposed inspiring further research for novel truly nanoscale optical sources with efficient pumping schemes. While incoherent sources of surface plasmon polaritons (SPPs) can be relatively easily integrated in a nanophotonic circuitry [1, 16, 17], the situation is more complicated in the case of coherent SPP sources and amplifiers, since to reach the lasing threshold one has to compensate not only Joule but also radiation losses, which can be quite large due to a small mode volume of the plasmonic cavity [13, 18]. The threshold gain may become very high, posing a serious challenge for the creation of the required population inversion. Although full compensation of the SPP losses at the nanoscale has been demonstrated [19–24], it was achieved under optical pumping, which is hardly compatible with on-chip integration [25–28], the target area of prospective applications. In this regard, an electrical pumping scheme is undeniably more desired and must be developed for practical application of plasmonic components [25, 26, 29, 30].

*Corresponding author: **Dmitry Yu. Fedyanin**, Laboratory of Nanooptics and Plasmonics, Center for Photonics and 2D Materials, Moscow Institute of Physics and Technology, 9 Institutsky Lane, Dolgoprudny 141700, Russian Federation, E-mail: dmitry.fedyanin@phystech.edu. <https://orcid.org/0000-0001-7264-0726>

Alexey V. Krasavin and Anatoly V. Zayats: Department of Physics and London Centre for Nanotechnology, King's College London, Strand, London WC2R 2LS, UK. <https://orcid.org/0000-0003-2522-5735> (A.V. Krasavin). <https://orcid.org/0000-0003-0566-4087> (A.V. Zayats)

Aleksey V. Arsenin: Laboratory of Nanooptics and Plasmonics, Center for Photonics and 2D Materials, Moscow Institute of Physics and Technology, 9 Institutsky Lane, Dolgoprudny 141700, Russian Federation. <https://orcid.org/0000-0002-7506-4389>

The possibility to implement electrical pumping in plasmonic devices is strongly restrained by a very limited choice of low-loss plasmonic metals. Gold, silver and copper form rectifying Schottky contacts to direct-bandgap semiconductors [31], while low-resistance ohmic contacts are needed for efficient electron and hole injection and creation of the population inversion in the gain medium [25, 32]. Therefore, one has to use ohmic contacts made of highly absorptive materials (such as titanium, chromium, palladium, and different alloys [25, 26, 33–35]), place it at a large distance from the active region of the structure and rely on the refractive index contrast between semiconductor materials to localize the optical mode and prevent its overlap with the ohmic contact [33, 35]. On the other hand, many proposed nanolaser designs based on low-absorptive structures (see, for example, Refs. [36–38]) can hardly be pumped electrically due to the high-resistance of metal-semiconductor contacts, which does not allow to inject a sufficient number of electrons and holes into the gain medium for the creation of the population inversion and full compensation of the high optical losses of the lasing mode. The high-resistance contact limitation greatly complicates the design of electrically pumped nanolasers and increases their physical size compared to the optically pumped counterparts. To overcome this problem, it was proposed to use the minority carrier injection properties of Schottky contacts and inject electrons into the gain semiconductor medium directly from the plasmonic metal, avoiding the commonly used intermediate semiconductor electron injection layer [27, 30]. However, there is only one binary III–V semiconductor material (InAs) that forms Schottky contacts to plasmonic metals with a barrier height greater than the bandgap energy of the semiconductor [31, 39], which is required for the creation of the population inversion [27, 30]. This limits the operation wavelength to around 3 μm and the operation temperature to below 150 K [40]. In addition, the inability of the Schottky barrier to block the majority carriers under forward bias leads to a quite high leakage current even in the presence of a single heterostructure [30], which greatly limits the energy efficiency of the amplification scheme.

Here, we propose an efficient electrically driven single-mode deep-subwavelength coherent optical source featuring a unique combination of strong nanophotonic guiding and a novel amplification scheme based on a double-heterostructure tunneling Schottky barrier diode, which gives the possibility to naturally implement electrical pumping by using the SPP supporting interface as a low-resistance n-type tunneling contact. This approach allows

dramatic reduction of the physical size of the device, simplifies its design, ensures in-plane emission and increases the operating temperature to above 300 K. Contrary to the electrically pumped metal coated nanopillar lasers [26, 33, 35, 41], which radiate photons into free space in a dipole-like fashion, the proposed SPP source is intrinsically integrable with nanophotonic circuitry. Unlike nanolasers based on localized optical modes, which are difficult to pump electrically [42], the subwavelength size of the proposed electrical SPP source is achieved with a propagating plasmonic mode, and the device can be referred as a SPPASER (surface plasmon polariton amplification by stimulated emission of radiation) or an SPP spaser [43]. The proposed approach enables the SPP to be efficiently out-coupled to a bus plasmonic or photonic waveguide without losing energy through the emission into the surrounding space, which is particularly important in large-scale integrated nanophotonic circuits, where performance and scalability are limited by the crosstalk noise.

2 Results and discussion

2.1 Implementation of electrical pumping

The proposed amplification scheme based on the Au/n⁺-InAs_{0.4}P_{0.6}/In_{0.72}Ga_{0.28}As/p⁺-Al_{0.29}In_{0.71}As double-heterostructure tunneling Schottky barrier diode is shown in Figure 1 (see Supplementary Information Section 1 for details). It gives the possibility to use the low-loss SPP supporting interface between gold and the 100-nm-thick electron injection n⁺-InAsP layer as a low-resistance tunneling contact to the n⁺-InAsP electron injection layer with nearly ideal ohmic characteristics. Therefore, the material gain in InGaAs is provided in the near-field proximity to the gold contact, exactly where the plasmonic modes are localized, which gives a crucial advantage over traditional electrical pumpings schemes of plasmonic and photonic nanolasers based on highly absorptive ohmic contacts [29, 33, 35, 41, 44]. The n-doped InGaAs layer sandwiched between the p⁺-AlInAs and n⁺-InAsP layers with bandgap energies exceeding that of InGaAs acts as an active region of the semiconductor structure. Under high forward bias, electrons and holes are injected into InGaAs from the InAsP and AlInAs sides, respectively, while high potential barriers for electrons at the InGaAs/AlInAs heterojunction and for holes at the InAsP/InGaAs heterojunction confine excess carriers to the active InGaAs region, which gives the double-heterostructure tunneling Schottky barrier diode amplification scheme a significant advantage over the amplification schemes based on

Schottky diodes, which suffer from high leakage currents [27, 30, 40]. Although the Au/n-InP Schottky barrier is as high as 0.5 eV [31], the Fermi level in Au/InAs contacts is anomalously pinned to the conduction band of InAs [31, 45]. Therefore, a wide range of InAsP ternary alloys form contacts to gold with a quite small barrier height. In particular, the height of the Au/n-InAs_{0.4}P_{0.6} barrier does not exceed 0.2 eV [31, 46]. The barrier width is determined by the density of donors and is equal to only 13 nm at a moderate doping level of $N_D^{\text{InAsP}} = 3 \times 10^{18} \text{ cm}^{-3}$. Electrons can easily tunnel through this barrier thanks to their extremely small effective mass ($0.057m_{e0}$) (see Supplementary Information Section 2). The evaluated specific contact resistance of the tunneling Au/n⁺-InAs_{0.4}P_{0.6} contact is as low as $1.2 \times 10^{-7} \text{ Ohm cm}^2$ (Methods). The voltage drop across the contact does not exceed 7 mV even at a pump current density of 50 kA/cm² (Figure 1c), which ensures nearly ideal ohmic characteristics of the Au/n-InAs_{0.4}P_{0.6} contact and efficient injection of electrons into the active InGaAs region. In comparison, InP, which would be used as an InGaAs lattice-matched material for the laser operation at 1.55 μm wavelength, with the same donor concentration of $3 \times 10^{18} \text{ cm}^{-3}$ forms a rectifying contact to gold (see Supplementary Information Section 2). Its contact resistance is two orders of magnitude higher than that of the Au/n⁺-InAs_{0.4}P_{0.6} contact, which results in high heat dissipation, which does not allow to use the Au/InP contact for electrical pumping of metal-semiconductor nanolasers at room temperature. In other words, the performance of the proposed amplification scheme is much better than that based on compound semiconductors lattice-matched to InP.

2.2 Design of the nanolaser cavity

An essential component of the coherent SPP source is a cavity. Here, we use a subwavelength ring-resonator design based on a T-shaped waveguiding geometry (Figure 1). The InAsP/InGaAs/AlInAs layer stack on AlInAs is ring-shaped and surrounded by silicon oxide, while a gold superstrate completes the cavity structure and forms an SPP supporting interface. The ring width $w = 300 \text{ nm}$ is designed to be about 7 times smaller than the source operating wavelength to provide high lateral confinement of plasmonic modes propagating along the metal-semiconductor interface of the ring resonator. The ring width can be easily decreased below $\lambda/10$, but this procedure does not noticeably improve the mode localization or even deteriorates it, whereas the bending losses are substantially magnified due to the decrease in the mode effective index. The ring height of 1 μm is smaller than the light wavelengths in the targeted spectral region, compelling parasitic photonic modes to leak into the semiconductor substrate with a high refractive index. At the same time, the height is large enough to prevent strongly localized SPP modes from undesirable radiation losses. The resulting aspect ratio between the ring height H and the ring width w is 3.3:1 that should not present any problem for the device fabrication [47]. The thickness of the electron injection InAsP layer is chosen to be 50 nm, which is significantly greater than the depletion layer thickness of the Au/n⁺-InAsP contact (13 nm) and allows efficient electron injection into the active InGaAs region. At the same time, the InGaAs layer is set to be 350 nm thick to provide more than 74% confinement of the plasmonic modes to the active InGaAs region to reduce the threshold gain

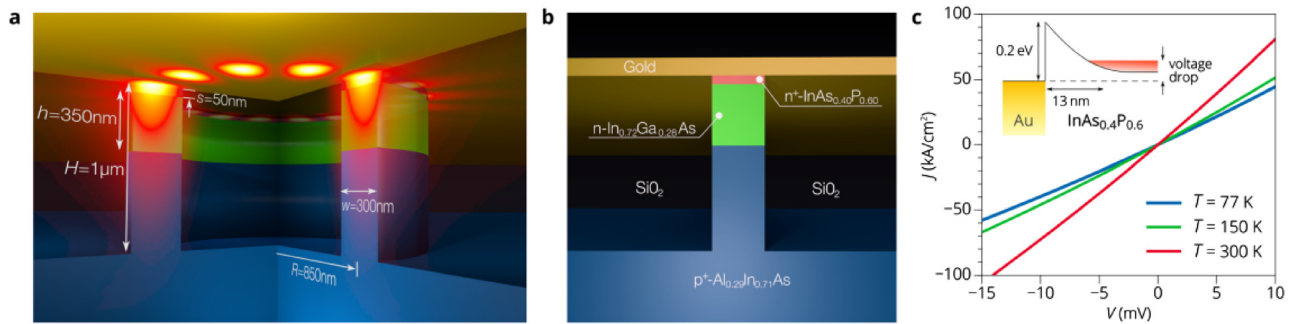


Figure 1: (a) Schematic of the ring resonator of the electrically driven coherent surface plasmon polariton (SPP) source based on a T-shaped plasmonic waveguide. The simulated electric field intensity ($|E|^2$) distribution of the SPP mode is overlaid on the geometry. (b) Cross-section of the T-shaped plasmonic waveguide. The relevant geometrical parameters of the device are also indicated: R is the radius of the ring, H and w are the height and the width of the waveguide, respectively, s is the thickness of the electron injection layer, and h is the height of the active region. Doping densities of the lattice-matched n⁺-InAs_{0.4}P_{0.6}, n-In_{0.72}Ga_{0.28}As, and p⁺-Al_{0.29}In_{0.71}As layers are $3 \times 10^{18} \text{ cm}^{-3}$, $3.1 \times 10^{15} \text{ cm}^{-3}$, and $4.4 \times 10^{18} \text{ cm}^{-3}$, respectively. (c) Current–voltage characteristics of the Au/n⁺-InAs_{0.4}P_{0.6} tunneling Schottky contact at room and low temperatures. Inset: schematic illustration of the barrier for electrons at the metal/semiconductor interface.

(Methods). The ring radius $R = 0.85 \mu\text{m}$ is selected so that one of the fundamental plasmonic modes of the ring resonator is close to the maximum of the gain spectrum of InGaAs at both room and low temperatures. Finally, we note that the proposed pumping scheme is universal and can also be used with other types of resonators.

Figure 2 shows the device mode structure at room temperature, obtained using the three-dimensional eigenmode simulations (Methods). Five types of modes (TM_{00} , TE_{00} , TM_{01} , TE_{01} , and TM_{10}) with the quality factors (Q -factors) greater than 10 are supported by the resonator within the spontaneous emission bandwidth of InGaAs. Here, the Q -factor is defined as a ratio of the energy of the SPP stored in the resonator to the energy dissipated per radian of the oscillation. TE_{01} and TM_{10} modes having two maxima in the vertical direction are pushed out of the cross section of the ring waveguide and radiate into the substrate. Photonic TE_{00} modes are much better localized in the ring waveguide, but their mode effective indices are significantly lower than the refractive index of AlInAs, which leads to strong coupling to substrate radiation modes. As a result, the Q -factors of these modes are less than 50, corresponding to modal losses of more than 3000 cm^{-1} , which are too high to be compensated by InGaAs. It takes TE_{00} modes out of the competition for the gain since the highly localized plasmonic TM_{00} modes experience 5 times smaller losses and show a significant advantage in mode confinement to the active InGaAs region. Owing to the submicrometer radius of the ring resonator, the spectral spacing between the TM_{00} modes is of the order of the material gain bandwidth of InGaAs, which establishes favorable conditions for the single mode stimulated emission into the eighth order TM_{00} mode (TM_{00}^8 mode) with a frequency of 0.637 eV ($\lambda = 1.95 \mu\text{m}$ in free space). For the chosen ring radius of 850 nm, the resonator mode volume is only $0.033\lambda^3$, where λ is the free-space wavelength, and can be further reduced by decreasing the ring radius (Methods). However, it will result in the increase of emission into free space, while ideally, this process needs to be suppressed. Thus, the chosen ring radius ensures the ideal trade-off between the device footprint and performance. Finally, to achieve an integrated coherent SPP source, the electrically driven plasmonic resonator is coupled to a bus plasmonic waveguide of the same type, which serves as a device output (Figure 3a).

2.3 SPP nanolaser operation

To analyze the device operation, we have developed a self-consistent steady-state model describing the carrier

transport within the semiconductor, which comprises the Poisson equation connecting the electrostatic potential and the charge carrier densities, the drift-diffusion current equations, the electron and hole continuity equations and the rate equations for the resonator modes (Methods). These optoelectronic processes are simulated with the finite difference method combined in a self-consistent way with the finite element analysis of the excited optical modes, and hence the simulations take into account the Purcell effect and coupling to a bus waveguide in the rate equations (for details, see Supplementary Information Sections 5 and 6).

Figure 3 shows the results of the self-consistent optoelectronic simulations. Under a negative voltage applied to the top gold contact (forward bias), electrons and holes are injected into the active InGaAs region of the ring resonator and recombine there both radiatively (spontaneous and stimulated emission) and non-radiatively (Auger recombination) (Figure 3c). At small forward bias (not shown in Figure 3c), the recombination for the spontaneous emission exceeds the Auger recombination, but the high threshold optical gain requires high concentrations of nonequilibrium electrons and holes, and non-radiative processes begin to dominate over radiative ones as the bias increases. Eventually, more than 90% of the total current goes into the Auger recombination just below the threshold. The situation, however, changes dramatically above the threshold, when recombination due to stimulated emission into the spasing mode surpasses the other recombination processes (Figure 3c).

Despite the fact that the Q -factors of TM_{00}^7 , TM_{00}^8 , TM_{00}^9 , and TM_{00}^{10} are of the same order of magnitude (Figure 2a), internal absorption of InGaAs due to band-to-band and intervalence band transitions leads to a significant difference in the modal loss at zero bias (see Supplementary Information Section 4). The TM_{00}^7 mode being closer to the bandgap energy of InGaAs suffers less absorption and could be the first to reach the threshold, but the material gain spectrum of InGaAs changes as the electron and hole concentrations increase and its maximum is blue-shifted, which gives the TM_{00}^8 mode an advantage over the other modes (Figure 3f). At a current density of 8.4 kA/cm^2 , the output power of the TM_{00}^7 mode becomes smaller than that of the TM_{00}^8 mode and does not change appreciably henceforward (Figure 3b). The TM_{00}^9 and TM_{00}^{10} modes show behavior very similar to the TM_{00}^8 mode but do not reach the threshold.

In the light-current characteristic of the TM_{00}^8 mode at a current density of about 30 kA/cm^2 there is a well-pronounced amplified spontaneous (ASE) kink (the

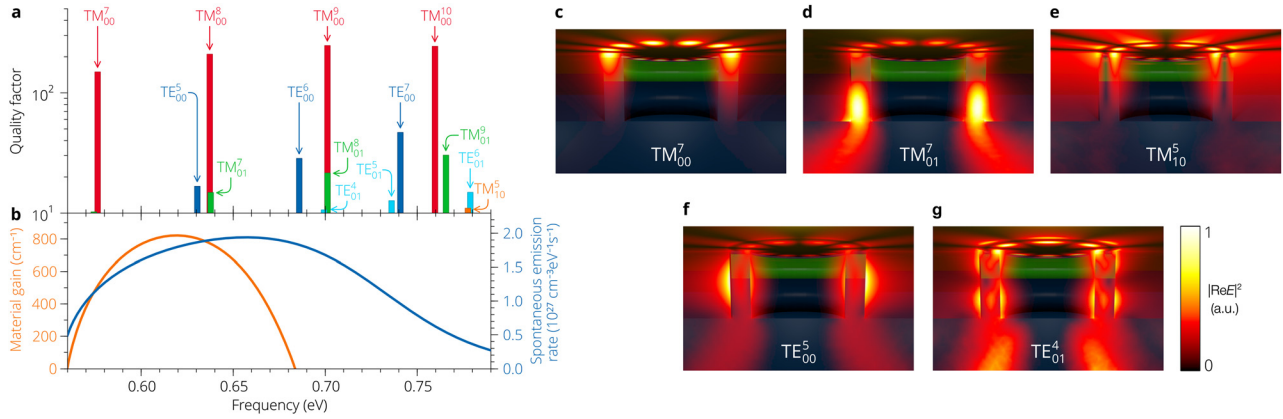


Figure 2: (a) The modal spectrum of the plasmonic resonator depicted in Figure 1. Modes are labeled so that two numbers in the subscript show the number of maxima in the radial and vertical directions and the superscript indicates the order of the mode, i.e., the number of wavelengths around the ring circumference. (b) Spontaneous emission and material gain spectra of bulk $\text{In}_{0.72}\text{Ga}_{0.28}\text{As}$ at room temperature (see Supplementary Information Section 4). (c–g) Simulated mode profiles of the electric field intensity for the TM_{00}^7 , TM_{01}^7 , TM_{10}^5 , TE_{00}^5 , and TE_{01}^4 modes, respectively. The spatial profile of the TM_{00}^8 mode is shown in Figure 1.

current at which the derivative of the slope of the curve of the output power versus injection current in a log-log scale changes its sign [48]). At this current, the recombination rate for the stimulated emission exceeds that for the spontaneous emission into all the resonator modes and into free space (Figure 3c,g). The pronounced ASE kink is explained by the fact that the spontaneous emission spectrum of bulk InGaAs is fairly broad (Figure 2b), which, combined with a moderate Purcell factor in the considered waveguiding geometry (see Supplementary Information Subsection 5.3), results primarily in emission into free space. The spontaneous emission coupling factor β ranges from 0.1 at small bias to 0.06 at high forward bias above the threshold. At $J = 30 \text{ kA/cm}^2$, the quality factor of the TM_{00}^8 mode is equal to 4700 corresponding to a sub-nanometer linewidth, which is extremely difficult to achieve at the nanoscale [35].

Due to the high β -factors, the emission properties of nanolasers are remarkably different from that of macroscopic lasers [49, 50], the ASE kink by itself does not guarantee that the output radiation is coherent right above it [49], while coherence is the most important and distinct feature of laser radiation. Also, it has been shown that the ASE kink in the light-current characteristic cannot be a measure of the threshold [48, 49]. To find the spasing threshold of the TM_{00}^8 mode, one should use the definition of the threshold based on the degree of the second-order coherence of the output radiation [49]. The calculations show that the threshold current density is equal to 47 kA/cm^2 , which is slightly higher than the current density of the ASE kink (Methods). The output power of the TM_{00}^8 mode at the threshold is $29 \mu\text{W}$, while the output powers of the TM_{00}^7

and TM_{00}^9 modes are 100 and 300 times lower, respectively. The powers of TE_{00} , TM_{01} , TE_{01} , and TM_{10} modes are even smaller than that of the spurious TM_{00}^9 mode. Thus, single-mode spasing is achieved.

At low temperatures, the device performance is greatly improved due to the decrease in the non-radiative recombination rate, since the threshold gain is achieved at a significantly smaller carrier concentration, and the Auger recombination coefficient in InGaAs is reduced from $3.8 \times 10^{-28} \text{ cm}^6 \text{ s}^{-1}$ at 300 K to $1.2 \times 10^{-28} \text{ cm}^6 \text{ s}^{-1}$ at 150 K and to about $2 \times 10^{-29} \text{ cm}^6 \text{ s}^{-1}$ at 77 K [51]. In addition, the electron-phonon scattering rate in gold γ_{ph} decreases as the temperature decreases [30, 52]. Accordingly, the imaginary part of the permittivity of the 100-nm-thick gold film at a frequency of 0.65 eV is reduced by a factor of 1.35 and 1.6 and equals $\epsilon''_{\text{Au}} = 9.5$ and $\epsilon''_{\text{Au}} = 8.0$ at 150 K and 77 K, respectively (see Supplementary Information Subsection 3.2). This leads to the increase of the Q -factor of the TM_{00}^8 mode to 260 at 150 K and 290 at 77 K, compared to $Q = 210$ at room temperature. The temperature decrease induces broadening of the semiconductor bandgap and, consequently, the corresponding shift of the material gain spectrum (Figure 4a). As a result, at 150 K, the TM_{00}^7 mode with a frequency of 0.582 eV is now outside the amplification bandwidth of InGaAs. The Auger recombination rate dramatically decreases, and, below the threshold, most of the current contributes to spontaneous emission. The spontaneous emission spectrum is narrower than at 300 K, and the β -factor is twice larger (from 0.16 to 0.20 depending on the bias voltage). The current at which the ASE kink is observed, is equal to $J_{\text{ASE}} = 1.1 \text{ kA/cm}^2$. However, the light-current characteristic demonstrates a very smooth

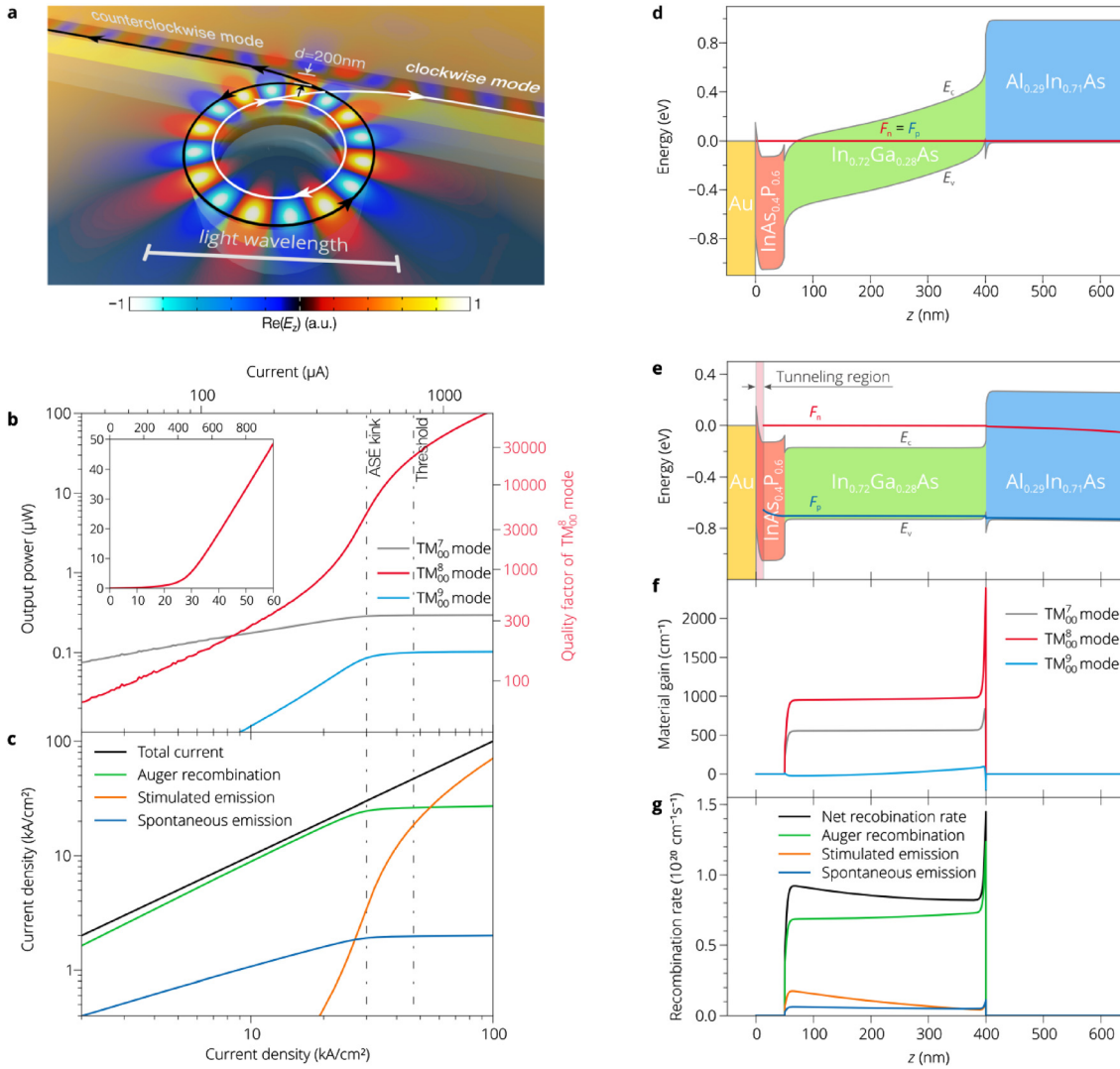


Figure 3: (a) Schematic of the coherent SPP source consisting of the subwavelength ring resonator shown in Figure 1, coupled to the straight plasmonic waveguide having the same width as the ring waveguide. The field map shows the simulated electric field distribution of the spasing TM_{00}^8 mode, which is doubly degenerated, and therefore the source emits SPPs with the same amplitude in both directions of the bus waveguide. The 200 nm gap between the waveguide and ring resonator corresponds to an intensity coupling coefficient of 5.6% for the TM_{00}^8 mode (see Supplementary Information Section 6.2). (b) Output power at the waveguide and Q -factor of the TM_{00}^8 mode versus injection current at room temperature. Note that the Q -factor is directly connected to the linewidth of the SPP source only below the threshold. Inset: a linear plot of the output power as a function of the injection current near the threshold region. (c) Contribution of different recombination processes (Auger recombination, spontaneous emission and stimulated emission) to the total current. (d) Energy band diagram of the double-heterostructure tunneling Schottky barrier diode along the z (vertical) direction in equilibrium. (e–g) Energy band diagram, material gain and recombination rate profiles along the z direction at a current density of 30 kA/cm².

transition from spontaneous to stimulated emission, which is typical for high- β lasers [48, 53]. At the same time, the stimulated emission rate exceeds the rate of the spontaneous emission into the spasing TM_{00}^8 mode at $J_{st-sp} = 660$ A/cm², which is 45 times lower than at room temperature. Interestingly, the threshold current does not decrease dramatically as temperature decreases, since the coherence of the nanolaser radiation is determined by the fluctuations in the free carrier densities in the gain

medium, which cannot be reduced by orders of magnitude [49]. At 150 K, the threshold current density is equal to $J_{th} = 26$ kA/cm². At 77 K, the light-current characteristic is even smoother than at 150 K and the amplified spontaneous emission kink in the curve for the TM_{00}^8 mode is shifted to lower values of the injection current ($J_{ASE} = 115$ A/cm²). The Auger recombination rate becomes negligibly small and does not have any impact on the output characteristics. The β -factor increases to 0.36. The

rate of stimulated emission exceeds the rate of spontaneous emission at $J_{\text{st-sp}} = 290 \text{ A/cm}^2$, which is only twice lower than at 150 K. At the same time, the threshold current density is almost the same as at 150 K and is equal to 20 kA/cm^2 , which is typical for nearly thresholdless nanolasers [49].

2.4 Efficiency of the SPP ring nanolaser

Power consumption plays a decisive role in the viability of nanolasers [42]. Generally, high Joule losses in a plasmonic resonator present a serious challenge for obtaining a large efficiency of electro-optical conversion since a significant portion of the generated SPP quanta is absorbed by the metal rather than emitted into the waveguide. In addition, at room temperature, due to the high threshold carrier concentration, non-radiative Auger recombination still

gives a significant contribution to the total current above the threshold (Figure 3c). Nevertheless, in the proposed scheme, the energy efficiency (the ratio of the output power to the input electrical power) above the threshold is between 7% and 9% depending on the pump current, which is higher than for the state-of-the-art electrically pumped photonic-crystal nanocavity lasers [54, 55]. Decreasing the operating temperature dramatically improves characteristics of the proposed SPP nanolaser. At 150 K, the electro-optical conversion efficiency exceeds 16%, which is comparable with the best semiconductor lasers integrated on a chip [56, 57]. At cryogenic temperatures, the efficiency is improved to about 20%. This is mainly the result of the fundamental relation between spontaneous and stimulated emission into the spasing mode.

The energy efficiency can be further enhanced by optimizing the geometry of the SPP nanolaser. Particularly, by changing the separation distance d between the ring resonator and the bus waveguide, one can significantly increase the ratio of the output power at the bus waveguide to the power flow in the ring. As the separation distance d is decreased to 100 nm, the efficiency of electro-optical conversion at 150 K rises to 37% and is even higher at lower temperatures. With the further decrease of the separation distance, the coupling efficiency can be even higher [36]. However, at room temperature, this does not provide any real advantages, since a higher coupling coefficient corresponds to higher modal loss, which substantially increases the threshold current.

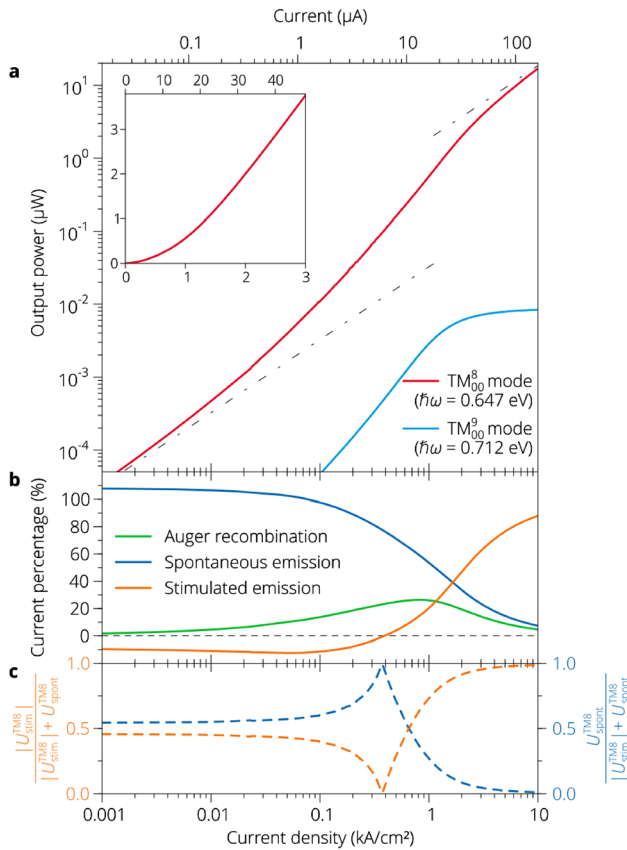


Figure 4: (a) Light-current characteristics of the SPP source at 150 K. (b) Contribution of various recombination processes (Auger recombination, surface recombination, spontaneous emission, and stimulated emission) in the total current. It should be noted that the contribution of the current related to the stimulated emission to the total current is negative under small forward bias, since absorption in the semiconductor dominates over stimulated emission. (c) Relation between the stimulated ($U_{\text{stim}}^{\text{TM}_0^8}$) and spontaneous ($U_{\text{spont}}^{\text{TM}_0^8}$) emission rates into the TM_{00}^8 mode.

3 Conclusion

The scheme proposed here for SPP amplification in deep-subwavelength plasmonic waveguides with integrated electrical pumping, based on a double heterostructure tunneling Schottky barrier diode, provides a realistic design of an electrically driven subwavelength coherent SPP source with dimensions orders of magnitude smaller than the typical size of in-plane coherent optical sources integrated on a chip [25, 56, 58], which are hardly compatible with nanophotonic circuitry. At the same time, unlike electrically pumped metal-coated nanolasers [26, 33, 35], the presented device does not merely emit light into free space in a dipole-like fashion, but efficiently couples the radiation into an in-plane plasmonic waveguide. It can also be directly coupled to a bus photonic semiconductor waveguide, which provides the compatibility with a standard low-loss photonic circuitry. The latter, however, comes at a price of smaller output power due to the increased scattering losses underlined by the spatial modal

mismatch between the plasmonic (ring) and the photonic waveguides (see Supplementary Information Section 7). The gold/semiconductor contact plays a dual role of the SPP supporting interface and the electron injection electrode, which eliminates the need for any additional electrical contacts, minimizing the device footprint and greatly facilitating the design of large-scale circuits. The vertical injection scheme, large band-edge offsets at the heterojunctions, and very low resistivity of the tunneling Au/n⁺-InAsP Schottky contact provide favorable conditions for efficient carrier injection into the active layer and minimize the leakage current, which is limited to the trap-assisted recombination at the interfaces. In contrast to most of light-emitting nanophotonic devices, the surface recombination does not play a significant role in the lattice matched InAs_{0.4}P_{0.6}/In_{0.72}Ga_{0.28}As/Al_{0.29}In_{0.71}As system thanks to a very small surface recombination velocity (2×10^3 cm/s) [59] combined with the low surface-to-volume ratio of the active region. At room temperature, the threshold current is determined by the non-radiative Auger recombination (for details on the effect of surface recombination, see Supplementary Information Section 7). Above the threshold, the contribution of surface recombination to the total current does not exceed 1.5%. In this aspect, the proposed configuration of the active region and the proper material choice provide a remarkable advantage over the tensile strained multiple quantum wells, which, in principle, can also serve as a gain medium [44], but are characterized by much greater area of the interfaces, substantially higher surface recombination velocities due to the increased density of surface defects and poorer confinement of the SPP field to the active region. Here, we should note that poor-quality interfaces may give rise to the surface density of trapping centers and increase the surface recombination velocity up to $\sim 1 \times 10^4$ cm/s. Nevertheless, our simulations demonstrate that even in this case, at room temperature, the contribution of surface recombination will not exceed 3 kA/cm² at the threshold, which is only about 10% of the total current.

The presented SPP source demonstrates remarkable characteristics, which can be further improved by structural and material optimization. Under room temperature conditions, the threshold is achieved at a moderate current density of 47 kA/cm², ensuring continuous-wave operation. The output power of up to 100 μ W at the energy efficiency of 8% is high enough to be used in future on-chip optical interconnects [60]. This makes the proposed SPP nanolaser superior to electrically driven photonic-crystal nanocavity lasers, which are much more complicated in fabrication and are characterized by a significantly smaller output power despite the lower threshold currents [54, 55]. As temperature

decreases, the device performance is dramatically enhanced. At temperatures below 150 K, the energy efficiency increases to above 17% and can be further improved to more than 35% by decreasing the separation distance between the output waveguide and the resonator to 100 nm, which makes it comparable with the energy efficiency of the best external semiconductor lasers. The proposed pumping scheme provides a strong basis for the design and development of electrically pumped active plasmonic waveguides that ensure lossless SPP guiding at the nanoscale, subdiffraction-limited electrically-driven SPP nanolasers for on-chip optical interconnects or large-scale nanophotonic and plasmonic circuits. Using heterogeneous integration (either hybrid integration based die-to-wafer bonding [25] or direct monolithic integration based on heteroepitaxy [61, 62]), these nanolasers can also be integrated with silicon waveguides, providing highly efficient electrically-driven on-chip coherent sources for various nanophotonic applications.

4 Methods

4.1 Self-consistent optoelectronic simulations

The proposed SPP source is simulated using the developed comprehensive self-consistent steady-state hybrid electronic/photonic model, which comprises six first order nonlinear differential equations describing the carrier behavior within the semiconductor (see Equation (S35) in Supplementary Information) and M integral rate equations for M optical modes of the plasmonic resonator (see Equation (S51) in Supplementary Information), coupled with the eigenmode FEM optical simulations (see Supplementary Information Subsection 6.2). The carrier transport equations include the Poisson equation (treated as two first order differential equations) connecting the electrostatic potential and the carrier densities, the drift-diffusion current equations and the electron and hole continuity equations. The carrier continuity equations cover processes of carrier generation and recombination, namely non-radiative Auger recombination, spontaneous emission into free space and into the resonator modes enhanced by the Purcell effect and stimulated emission. The latter connects the differential equation for carrier transport with the integral rate equations for the resonator modes. At the same time, the rate equations include the material gain and spontaneous emission into the resonator modes, which are obtained by integrating the transition probabilities between electron states in the conduction and valence bands over the states' energies. This introduces implicitly the electron and hole densities into M integral equations for the resonator modes.

Providing 18 boundary conditions at the material interfaces and using the electromagnetic field distributions of the resonator modes from the eigenmode optical simulations and the Purcell factor distribution from the 3D frequency domain FEM simulations (see Supplementary Information Subsection 5.3), the SPP source is self-consistently modeled using the finite difference method. The details on the optoelectronic model and simulations are described in Supplementary Information Section 6.

4.2 Electron transport through the tunneling Schottky contact

Tunneling and an over-barrier current across the metal-semiconductor contact is calculated using the exact solutions of the Schrödinger equation. The current density is given by

$$J = \frac{q\rho_{mf}}{m_{es}} \int_{-\infty}^{+\infty} dE [f(E - qV)] \times \int_0^{\pi/2} \sqrt{2(E - qV)m_{es} - (m_{em}v_{fm}\sin\theta)^2} |T_{m \rightarrow s}(\theta, E)|^2 \sin\theta d\theta, \quad (1)$$

where q is the electron charge, V is the voltage across the contact, m_{es} and m_{em} are the effective electron masses in the semiconductor and metal, respectively, $f(E)$ is the Fermi distribution function, v_{fm} is the Fermi velocity in the metal, ρ_{mf} is density of states in the metal at the Fermi energy, and $T_{m \rightarrow s}(\theta, E)$ is the barrier transmission coefficient calculated from an electron wave function (for details, see Supplementary Information Section 2).

4.3 Mode structure simulations

The set of modes supported by the plasmonic resonator is found via the 3D finite element method (FEM) numerical simulations using COMSOL Multiphysics software. The outer domain boundaries are placed at a large distance from the structure to ensure their position in the radiation zone, so that the radiative components of the fields escaped from the resonator are efficiently absorbed using perfectly matched layers. For each resonator mode, a complex eigenfrequency $\Omega = \omega + \delta \cdot i$ is determined, the real part of which defines the actual resonant frequency, while the imaginary part is responsible for losses. From these values, the resonator quality factor and the modal loss $\alpha = 2\delta/\nu_g$ are calculated. Here, ν_g is the group velocity of the corresponding optical mode of the waveguide of the ring resonator, which is found in the designated 2D FEM eigenmode simulations.

The dielectric function of gold used in the simulations is calculated taking into account electron-phonon, electron-electron, grain boundary and surface scattering, and verified by the experimental data. The temperature dependence of the dielectric function was determined considering the proper temperature variations of each scattering component. The dielectric functions of the compound semiconductors used in the simulations are calculated using the Clausius–Mossotti relation and their temperature dependences are obtained using an empirical model by Herve and Vandamme.

For details on the eigenmode simulations and the dielectric constants evaluation, see Supplementary Information Section 3.

4.4 Quality factor

The quality factor of the resonator is defined as a ratio of the energy stored in the resonator to the energy loss per radian of the oscillation [63]. To evaluate the Q -factor under electrical pumping, we use the results from 3D eigenmode simulations of the passive structure and self-consistent optoelectronic simulations, which give the modal loss of each mode of the resonator under applied bias (for details, see Supplementary Information Section 6).

4.5 Mode volume

The mode volume of the resonator mode is calculated using the data retrieved from the 3D eigenmode simulations [64]

$$V_{\text{eff}} = \frac{\int \varepsilon(\mathbf{r}) |E(\mathbf{r})|^2 d^3\mathbf{r}}{\max[\varepsilon(\mathbf{r}) |E(\mathbf{r})|^2]}, \quad (2)$$

where $E(\mathbf{r})$ is the complex amplitude of the electric field of the optical mode and the integration in the numerator is performed over the entire domain occupied by the mode.

4.6 Mode confinement to the active region

The confinement factor of the mode to the active region of the waveguide of the plasmonic ring resonator is determined as [65]:

$$\Gamma_{\text{active}} = \frac{c}{8\pi\nu_g} \frac{\text{Re}(n_{\text{InGaAs}}) \iint |E(x, z)|^2 dx dz}{\int_{-\infty}^{+\infty} \int_{-\infty}^{+\infty} W(x, z) dx dz}, \quad (3)$$

where $W(x, z)$ is the energy density of the optical mode, n_{InGaAs} is the refractive index of $\text{In}_{0.72}\text{Ga}_{0.28}\text{As}$, and ν_g is the mode group velocity. The integral in the numerator is taken over the active $\text{In}_{0.72}\text{Ga}_{0.28}\text{As}$ region, while the integration in the denominator is performed over the whole 2D domain occupied by the mode.

4.7 Purcell factor

The Purcell factor, defining the change in the spontaneous decay rate of an emitter located in the active region of the waveguide of the plasmonic ring resonator from its value in the corresponding uniform semiconductor, is calculated as a ratio of the power flows emitted by a dipolar emitter placed in the respective electromagnetic environments:

$$P(\mathbf{r}, \hbar\omega) = \frac{\text{Im}[\boldsymbol{\mu} \mathbf{E}_{\text{tot}}^{\text{wg}}(\mathbf{r}, \hbar\omega)]}{\text{Im}[\boldsymbol{\mu} \mathbf{E}_{\text{tot}}^{\text{inf}}(\hbar\omega)]}, \quad (4)$$

where $\boldsymbol{\mu}$ is the dipole moment, and $\mathbf{E}_{\text{tot}}^{\text{wg}}(\mathbf{r}, \hbar\omega)$ and $\mathbf{E}_{\text{tot}}^{\text{inf}}(\hbar\omega)$ are the total electric fields at the dipole position. To find the electric field values, a dedicated set of 3D frequency domain numerical simulations of the dipole emission was performed. Varying the dipole position and averaging the results over all its orientations, the full Purcell factor map of the active region is obtained (for details, see Supplementary Information Subsection 5.3).

4.8 Threshold current

The spasing threshold was found using its definition through the second-order coherence properties of the emission as the transition from the emission in the thermal state of light to the emission in the coherent state of light. The threshold current density is obtained by solving the following transcendental equation [49]:

$$J_{\text{th}} = q \sqrt{\frac{n_{\text{InGaAs}} V \omega^3}{\left. \frac{dG(J)}{d(n)(J)} \right|_{J=J_{\text{th}}} c Q_{\text{tot}}^3}}, \quad (5)$$

where V is the volume of the InGaAs active region, $G(J)$ is the modal gain of the spasing mode in the ring resonator, $\langle n \rangle(J)$ is the averaged

electron density in the InGaAs active region, ω is the angular frequency of the spasing mode, Q_{tot} is the quality factor of the spasing mode that includes losses due to coupling to a bus waveguide and q is the elementary charge.

Author contribution: All the authors have accepted responsibility for the entire content of this submitted manuscript and approved submission.

Research funding: D.Y.F. acknowledges support from the Russian Foundation for Basic Research (19-57-12008). A.V.K. and A.V.Z. acknowledge support from the Engineering and Physical Sciences Research Council (U.K.). A.V.A. acknowledges support from the Ministry of Science and Higher Education of the Russian Federation (0714-2020-0002). The development of the software for optoelectronic simulations was supported by the Russian Science Foundation (17-79-20421).

Conflict of interest statement: The authors declare no conflicts of interest regarding this article.

References

- [1] K. C. Y. Huang, M.-K. Seo, T. Sarmiento, Y. Huo, J. S. Harris, and M. L. Brongersma, "Electrically driven subwavelength optical nanocircuits," *Nat. Photonics*, vol. 8, pp. 244–249, 2014.
- [2] P. Wang, A. V. Krasavin, M. E. Nasir, W. Dickson, and A. V. Zayats, "Reactive tunnel junctions in electrically driven plasmonic nanorod metamaterials," *Nat. Nanotechnol.*, vol. 13, pp. 159–165, 2018.
- [3] B. C. Stipe, T. C. Strand, C. C. Poon, et al., "Magnetic recording at 1.5 Pb m^{-2} using an integrated plasmonic antenna," *Nat. Photonics*, vol. 4, pp. 484–488, 2010.
- [4] P. Wang, M. E. Nasir, A. V. Krasavin, W. Dickson, and A. V. Zayats, "Optoelectronic synapses based on hot-electron-induced chemical processes," *Nano Lett.*, vol. 20, pp. 1536–1541, 2020.
- [5] W. Heni, Y. Fedoryshyn, B. Baeuerle, et al., "Plasmonic IQ modulators with attojoule per bit electrical energy consumption," *Nat. Commun.*, vol. 10, no. 8, p. 1694, 2019.
- [6] A. V. Krasavin and A. V. Zayats, "Active nanophotonic circuitry based on dielectric-loaded plasmonic waveguides," *Adv. Opt. Mater.*, vol. 3, pp. 1662–1690, 2015.
- [7] C. Haffner, D. Chelladurai, Y. Fedoryshyn, et al., "Low-loss plasmon-assisted electro-optic modulator," *Nature*, vol. 556, pp. 483–486, 2018.
- [8] J. E. Muench, A. Ruocco, M. A. Giambra, et al., "Waveguide-integrated, plasmonic enhanced graphene photodetectors," *Nano Lett.*, vol. 19, pp. 7632–7644, 2019.
- [9] A. V. Krasavin and A. V. Zayats, "Benchmarking system-level performance of passive and active plasmonic components: integrated circuit approach," *Proc. IEEE*, vol. 104, pp. 2338–2348, 2016.
- [10] A. V. Krasavin, P. Wang, M. E. Nasir, Y. L. Jiang, and A. V. Zayats, "Tunneling-induced broadband and tunable optical emission from plasmonic nanorod metamaterials," *Nanophotonics*, vol. 9, pp. 427–434, 2020.
- [11] C. P. T. McPolin, J. S. Bouillard, S. Vilain, et al., "Integrated plasmonic circuitry on a vertical-cavity surface-emitting semiconductor laser platform," *Nat. Commun.*, vol. 7, no. 8, p. 12409, 2016.
- [12] C.-Z. Ning, "Semiconductor nanolasers and the size-energy-efficiency challenge: a review," *Adv. Photon.*, vol. 1, p. 014002, 2019.
- [13] R. M. Ma and R. F. Oulton, "Applications of nanolasers," *Nat. Nanotechnol.*, vol. 14, pp. 12–22, 2019.
- [14] D. J. Bergman and M. I. Stockman, "Surface plasmon amplification by stimulated emission of radiation: quantum generation of coherent surface plasmons in nanosystems," *Phys. Rev. Lett.*, vol. 90, p. 027402, 2003.
- [15] S. I. Azzam, A. V. Kildishev, R. M. Ma, et al., "Ten years of spasers and plasmonic nanolasers," *Light Sci. Appl.*, vol. 9, no. 21, p. 90, 2020.
- [16] R. J. Walters, R. V. van Loon, I. Brunets, J. Schmitz, and A. Polman, "A silicon-based electrical source of surface plasmon polaritons," *Nat. Mater.*, vol. 9, pp. 21–25, 2010.
- [17] D. M. Koller, A. Hohenau, H. Ditlbacher, et al., "Organic plasmon-emitting diode," *Nat. Photonics*, vol. 2, pp. 684–687, 2008.
- [18] S.-L. Wang, S. Wang, X.-K. Man, and R.-M. Ma, "Loss and gain in a plasmonic nanolaser," *Nanophotonics*, 2020, <https://doi.org/10.1515/nanoph-2020-0117>.
- [19] S. Kena-Cohen, P. N. Stavrinou, D. D. Bradley, and S. A. Maier, "Confined surface plasmon-polariton amplifiers," *Nano Lett.*, vol. 13, pp. 1323–1329, 2013.
- [20] C.-J. Lee, H. Yeh, F. Cheng, et al., "Low-threshold plasmonic lasers on a single-crystalline epitaxial silver platform at telecom wavelength," *ACS Photonics*, vol. 4, pp. 1431–1439, 2017.
- [21] R. F. Oulton, V. J. Sorger, T. Zentgraf, et al., "Plasmon lasers at deep subwavelength scale," *Nature*, vol. 461, pp. 629–632, 2009.
- [22] R. M. Ma, R. F. Oulton, V. J. Sorger, G. Bartal, and X. Zhang, "Room-temperature sub-diffraction-limited plasmon laser by total internal reflection," *Nat. Mater.*, vol. 10, pp. 110–113, 2011.
- [23] Y. L. Ho, J. K. Clark, A. Syazwan, A. Kamal, and J. J. Delaunay, "On-chip monolithically fabricated plasmonic-waveguide nanolaser," *Nano Lett.*, vol. 18, pp. 7769–7776, 2018.
- [24] C. Xu, W. E. Hayenga, M. Khajavikhan, and P. Likamwa, "Measuring the frequency response of optically pumped metal-clad nanolasers," *Opt. Express*, vol. 27, pp. 21834–21843, 2019.
- [25] A. W. Fang, H. Park, O. Cohen, R. Jones, M. J. Paniccia, and J. E. Bowers, "Electrically pumped hybrid algal-silicon evanescent laser," *Opt. Express*, vol. 14, pp. 9203–9210, 2006.
- [26] M. T. Hill, Y.-S. Oei, B. Smalbrugge, et al., "Lasing in metallic-coated nanocavities," *Nat. Photonics*, vol. 1, pp. 589–594, 2007.
- [27] D. Y. Fedyanin, "Toward an electrically pumped spaser," *Opt. Lett.*, vol. 37, pp. 404–406, 2012.
- [28] B. Romeira and A. Fiore, "Physical limits of nanoleds and nanolasers for optical communications," *Proc. IEEE*, vol. 108, pp. 735–748, 2020.
- [29] F. Vallini, Q. Gu, M. Kats, Y. Fainman, and N. C. Frateschi, "Carrier saturation in multiple quantum well metallo-dielectric semiconductor nanolaser: is bulk material a better choice for gain media?," *Opt. Express*, vol. 21, pp. 25985–25998, 2013.
- [30] D. Y. Fedyanin, A. V. Krasavin, A. V. Arsenin, and A. V. Zayats, "Surface plasmon polariton amplification upon electrical injection in highly integrated plasmonic circuits," *Nano Lett.*, vol. 12, pp. 2459–2463, 2012.

- [31] S. Tiwari and D. J. Frank, “Empirical fit to band discontinuities and barrier heights in III–V alloy systems,” *Appl. Phys. Lett.*, vol. 60, pp. 630–632, 1992.
- [32] Q. Gu and Y. Feinman, *Semiconductor Nanolasers*, Cambridge University Press, 2017.
- [33] M. T. Hill, M. Marell, E. S. P. Leong, et al., “Lasing in metal-insulator-metal sub-wavelength plasmonic waveguides,” *Opt. Express*, vol. 17, pp. 11107–11112, 2009.
- [34] G. Stareev, H. Künzel, and G. Dortmund, “A controllable mechanism of forming extremely low-resistance nonalloyed ohmic contacts to group III–V compound semiconductors,” *J. Appl. Phys.*, vol. 74, pp. 7344–7356, 1993.
- [35] K. Ding, M. T. Hill, Z. C. Liu, L. J. Yin, P. J. van Veldhoven, and C. Z. Ning, “Record performance of electrical injection sub-wavelength metallic-cavity semiconductor lasers at room temperature,” *Opt. Express*, vol. 21, pp. 4728–4733, 2013.
- [36] K. Liu, N. Li, D. K. Sadana, and V. J. Sorger, “Integrated nanocavity plasmon light sources for on-chip optical interconnects,” *ACS Photonics*, vol. 3, pp. 233–242, 2016.
- [37] D. B. Li and C. Z. Ning, “Interplay of various loss mechanisms and ultimate size limit of a surface plasmon polariton semiconductor nanolaser,” *Opt. Express*, vol. 20, pp. 16348–16357, 2012.
- [38] S. Wang, H. Z. Chen, and R. M. Ma, “High performance plasmonic nanolasers with external quantum efficiency exceeding 10,” *Nano Lett.*, vol. 18, pp. 7942–7948, 2018.
- [39] C. A. Mead and W. G. Spitzer, “Fermi level position at semiconductor surfaces,” *Phys. Rev. Lett.*, vol. 10, pp. 471–472, 1963.
- [40] A. A. Vyshnevyy and D. Y. Fedyanin, “Self-heating and cooling of active plasmonic waveguides,” *ACS Photonics*, vol. 3, pp. 51–57, 2016.
- [41] J. H. Lee, M. Khajavikhan, A. Simic, et al., “Electrically pumped sub-wavelength metallo-dielectric pedestal pillar lasers,” *Opt. Express*, vol. 19, pp. 21524–21531, 2011.
- [42] J. B. Khurgin and G. Sun, “Comparative analysis of spasers, vertical-cavity surface-emitting lasers and surface-plasmon-emitting diodes,” *Nat. Photonics*, vol. 8, pp. 468–473, 2014.
- [43] M. I. Stockman, “Nanoplasmonics: past, present, and glimpse into future,” *Opt. Express*, vol. 19, pp. 22029–22106, 2011.
- [44] D. Costantini, A. Bousseksou, M. Fevrier, B. Dagens, and R. Colombelli, “Loss and gain measurements of tensile-strained quantum well diode lasers for plasmonic devices at telecom wavelengths,” *IEEE J. Quantum Electron.*, vol. 48, pp. 73–78, 2012.
- [45] J. N. Walpole and K. W. Nill, “Capacitance-voltage characteristics of metal barriers on p PbTe and p InAs: effects of the inversion layer,” *J. Appl. Phys.*, vol. 42, pp. 5609–5617, 1971.
- [46] K. Kajiyama, Y. Mizushima, and S. Sakata, “Schottky barrier height of n-In_xGa_{1-x}As diodes,” *Appl. Phys. Lett.*, vol. 23, pp. 458–459, 1973.
- [47] R. Dylewicz, R. M. De La Rue, R. Wasielewski, P. Mazur, G. Mezósi, and A. C. Bryce, “Fabrication of submicron-sized features in InP/InGaAsP/AlGaInAs quantum well heterostructures by optimized inductively coupled plasma etching with Cl₂/Ar/N₂ chemistry,” *J. Vac. Sci. Technol. B*, vol. 28, pp. 882–890, 2010.
- [48] C. Z. Ning, “What is laser threshold?,” *IEEE J. Sel. Top. Quantum Electron.*, vol. 19, p. 1503604, 2013.
- [49] A. A. Vyshnevyy and D. Y. Fedyanin, “Lasing threshold of thresholdless and non-thresholdless metal-semiconductor nanolasers,” *Opt. Express*, vol. 26, pp. 33473–33483, 2018.
- [50] W. W. Chow, F. Jahnke, and C. Gies, “Emission properties of nanolasers during the transition to lasing,” *Light Sci. Appl.*, vol. 3, no. 8, p. e201, 2014.
- [51] T. H. Gfroerer, L. P. Priestley, M. F. Fairley, and M. W. Wanlass, “Temperature dependence of nonradiative recombination in low-band gap In_xGa_{1-x}As/InAs_yP_{1-y} double heterostructures grown on InP substrates,” *J. Appl. Phys.*, vol. 94, pp. 1738–1743, 2003.
- [52] J. S. Bouillard, W. Dickson, D. P. O’Connor, G. A. Wurtz, and A. V. Zayats, “Low-temperature plasmonics of metallic nanostructures,” *Nano Lett.*, vol. 12, pp. 1561–1565, 2012.
- [53] M. Khajavikhan, A. Simic, M. Katz, et al., “Thresholdless nanoscale coaxial lasers,” *Nature*, vol. 482, pp. 204–207, 2012.
- [54] K. Takeda, T. Sato, A. Shinya, et al., “Few-fj/bit data transmissions using directly modulated lambda-scale embedded active region photonic-crystal lasers,” *Nat. Photonics*, vol. 7, pp. 569–575, 2013.
- [55] K. Takeda, T. Sato, T. Fujii, et al., “Heterogeneously integrated photonic-crystal lasers on silicon for on/off chip optical interconnects,” *Opt. Express*, vol. 23, pp. 702–708, 2015.
- [56] B. R. Koch, E. J. Norberg, B. Kim, et al., “Integrated silicon photonic laser sources for telecom and datacom,” Optical Fiber Communication Conference/National Fiber Optic Engineers Conference 2013, OSA Technical Digest (online) (Optical Society of America, 2013), paper PDP5C.8, 2013, <https://doi.org/10.1364/ofc.2013.pdp5c.8>.
- [57] M. J. R. Heck and J. E. Bowers, “Energy efficient and energy proportional optical interconnects for multi-core processors: driving the need for on-chip sources,” *IEEE J. Sel. Top. Quantum Electron.*, vol. 20, pp. 332–343, 2014.
- [58] S. Chen, W. Li, J. Wu, et al., “Electrically pumped continuous-wave III–V quantum dot lasers on silicon,” *Nat. Photonics*, vol. 10, pp. 307–311, 2016.
- [59] J. R. Dixon, “Photoelectromagnetic effect in indium arsenide,” *Phys. Rev.*, vol. 107, pp. 374–378, 1957.
- [60] S. Manipatruni, M. Lipson, and I. A. Young, “Device scaling considerations for nanophotonic CMOS global interconnects,” *IEEE J. Sel. Top. Quantum Electron.*, vol. 19, p. 8200109, 2013.
- [61] E. Tournié, L. Cerutti, J.-B. Rodriguez, H. Liu, J. Wu, and S. Chen, “Metamorphic III–V semiconductor lasers grown on silicon,” *MRS Bulletin*, vol. 41, pp. 218–223, 2016.
- [62] Z. Wang, B. Tian, M. Pantouvaki, et al., “Room-temperature InP distributed feedback laser array directly grown on silicon,” *Nat. Photonics*, vol. 9, pp. 837–842, 2015.
- [63] K. Zhang and L. Dejie, *Electromagnetic Theory for Microwaves and Optoelectronics*, Springer-Verlag, 1998.
- [64] K. Srinivasan, M. Borselli, and O. Painter, “Cavity Q, mode volume, and lasing threshold in small diameter AlGaAs microdisks with embedded quantum dots,” *Opt. Express*, vol. 14, pp. 1094–1105, 2006.
- [65] T. D. Visser, H. Blok, B. Demeulenaere, and D. Lenstra, “Confinement factors and gain in optical amplifiers,” *IEEE J. Quantum Electron.*, vol. 33, pp. 1763–1766, 1997.

Supplementary material: The online version of this article offers supplementary material (<https://doi.org/10.1515/nanoph-2020-0157>).